Hierarchical Design and Development of Nanostructured Trifunctional Catalysts for Electrochemical Oxygen and Hydrogen Reactions

Huijuan Han[a,b], Zhengyu Bai[a,]*, Tao Zhang[c], Xiaobing Wang[a], Xiaoli Yang[a], Xiaoming Ma[a], Yuping Zhang[b], Lin Yang[a,]* Jun Lu [c,]*

[a] Collaborative Innovation Center of Henan Province for Green Manufacturing of Fine Chemicals, Henan Key Laboratory of Boron Chemistry and Advanced Energy Materials, Key Laboratory of Green Chemical Media and Reactions, Ministry of Education, School of Chemistry and Chemical Engineering, Henan Normal University, Xinxiang, Henan 453007, P. R. China.

[b] School of Chemistry and Chemical Engineering, Henan Institute of Science and Technology, Xinxiang 453003, P. R. China.

[c] Chemical Sciences and Engineering Division, Argonne National Laboratory, Argonne, Illinois 60439, United States

***Corresponding Author:** baizhengyu@htu.cn(Z Bai); yanglin1819@163.com (L, Yang); junlu@anl.gov (J. Lu)

Abstract: Trifunctional catalysts show a great potential for use in a power-to-gas water-splitting devices for hydrogen gas production, powered by an integrated rechargeable zinc-air battery. None of the currently available commercial electrocatalysts is low cost, and they do not possess excellent catalytic activity and durability at the same time, which is the main barrier to the broad implementation of these technologies. Herein, we design and develop a novel nanostructured trifunctional electrocatalyst that is capable of catalyzing oxygen/hydrogen evolution and oxygen reduction reactions. The combination of non-precious Co, Co_9S_8, and S, N co-doped graphitic carbon synergistically provides highly active sites for efficient catalytic reactions, while the unique tubular morphology and hierarchically porous microstructure not only benefit fast access to active sites but also ensure a robust composite structure for durability. When applied to zinc-air batteries and water splitting, these systems exhibit performance superior to those of commercial precious electrocatalysts (e.g., Pt/C and Ir/C).

Keywords: nanomaterials; trifunctional catalysts; zinc-air battery; oxygen/hydrogen evolution; oxygen reduction reactions

1. Introduction

It is critically important to develop cheap, highly efficient, long-lasting, and eco-friendly electrocatalysts that, owing a broad range of functionality, meet the requirements of three key electrochemical processes, namely, the oxygen/hydrogen evolution reactions (OER/HER) and the oxygen reduction reaction (ORR), for improvement of renewable energy conversion and storage.[1-5] Rechargeable zinc-air batteries (ZnABs) (involving OER and ORR) and the water-splitting process (involving OER and HER) are typical examples. Currently, noble-metal catalysts are utilized for these fundamental electrochemical reactions, such as an Ir-based catalyst for OER and a Pt-based catalyst for HER and ORR. However, the high cost of the precious-metal-based catalysts has greatly limited the distribution and the commercialization of renewable energy technologies. [6-9]

To replace these precious-metal-based catalysts, many non-precious-metal-based catalysts have been reported for ORR, OER, or HER. Relevant research has revealed that carbon networks doped or co-doped with the insertion of heteroatoms (such as S and N) used as efficient electrocatalysts[10-15] and nanostructured transition-metal alloys or transition-metal (Fe, Co, and Ni) sulfides have exhibited promising performance as OER or HER catalysts. [16-18] Among these transition-metal chalcogenides, particularly cobalt pentlandite (Co_9S_8) catalysts, have been studied as a promising alternative to precious-metal-based catalysts in both acidic and alkaline mediums by academia and have attracted the most attention. [19]

However, the instinctual low conductivity, the severe aggregations of nanoparticles, and the complicated preparation procedures of Co_9S_8 have prohibited the full utilization of its electrocatalytic activity. [20-25] Therefore, many efforts have been devoted to solving these

problems. It has been reported that electrocatalytic activity was prominently enhanced by one-dimensional (1D) porous carbon, owing to the effective improvement of the interfacial contact between electrode − electrolyte and the transmission of ions and electrons, core-shell nanoparticles (NPs) often exhibit good catalytic performance in a variety of reactions. [26] Thus, our strategy is to design and synthesize a hybrid nanostructure that combines 1D S, N co-doped carbon nanomaterial with Co, Co_9S_8 core-shell nanoparticles as an electrocatalyst to effectively improve performance because the synergistic effects between Co, Co_9S_8, and heteroatoms co-doped in a 1D porous graphitic carbon matrix can improve the conductivity, durability, and electrochemical activity of the resulting catalysts.[22]Theoretical research shows that the electrocatalytic activity is strongly dependent on the heteroatom type and doping level. [27-29] It is very challenging to realize a carbon network doped with heteroatoms precisely with repeatability and controllability and forming hybrid 1D porous nanostructures. Currently, porous metal-organic frameworks (MOFs) with different architectures are the promising precursors of electrocatalysts. Owing to their particular structures and compositions, diverse architectures promoting electrocatalytic activity are a major source of the inspiration behind the present paper. [30-32]

In this work, we successfully fabricated hierarchical hybrid porous tubular nanostructures composed of core-shell nanoparticles with a Co-Co_9S_8 core and a graphitic carbon shell co-doped with S and N (Co-Co_9S_8@SN-CNTs) for the first time to the best of our knowledge. We used 1D cobalt-based metal-organic frameworks (Co-MOFs) as both self-templates and precursors. Our research results show that the Co-Co_9S_8@SN-CNTs obtained at a pyrolysis temperature of 900° C (Co-Co_9S_8@SN-CNTs-900) exhibit

superior ORR, OER, and HER performance and a high surface area (345 m^2 g^{-1}). The hybrid nanostructures show higher maximum power density (93 mW cm^{-2}) and better cycling stability in ZnABs. The obtained Co-Co_9S_8@SN-CNTs were also used as electrodes for full water splitting and displayed good performance and excellent stability for more than 15 h. The superior performance of the hierarchical hybrid 1D nanostructures is mainly attributed to the synergy between 1D porous nanostructures, core-shell nanostructures, and more active sites. Furthermore, it could be also attributed to the appropriate doping level of heteroatoms and the unique morphology and nanostructure of the electrocatalyst. This work provides a new and simple method for the preparation of 1D hybrid nanostructures composed of core-shell nanoparticles with superior performance.

2. Result and discussion

2.1Formation process of Co-Co_9S_8@SN-CNTs-900 catalyst

Scheme 1 shows the synthesis process of the Co-Co_9S_8@SN-CNTs-900. Bpy and Tdc were used as dual organic ligands to prepare [Co(Tdc)(Bpy)]n MOFs via a convenient hydrothermal method. The as-prepared S,N-containing 1D Co-MOFs offer the possibility of assembling 1D Co-based carbon materials co-doped with S and N for electrocatalysis applications. Herein, both Bpy and Tdc play a critical role in formation of 1D Co-MOF precursor. Meanwhile, the two ligands supply the C, S, and N sources. Next, the Co-Co_9S_8@SN-CNTs obtained by pyrolysis of the Co-MOFs in Ar, the S,N co-doped materials combined with crystalline Co and Co_9S_8 as the double core, and the graphitic carbon co-doped with S and N as the shell, are provided for electrocatalysis through a simple pyrolysis approach. For comparison, the Co-MOFs were

separately pyrolyzed at 600 ºC, 700 ºC, 800 ºC, and 900 ºC for 180 min each. The resulting products were represented as Co-MOF-600, Co@SN-CNTs-700, Co@SN-CNTs-800, and Co-Co_9S_8@SN-CNTs-900, respectively. The electrochemical test results reveal that the Co-Co_9S_8@SN-CNTs-900 shows the best electrochemical catalytic performance among the four resulting products.

2.2 Material characterization

Both FESEM and TEM were used to characterize the morphology of the Co-Co_9S_8@SN-CNTs-900 catalyst. As shown in Figure 1a, the surface of the carbon nanotube consists of many small nanoparticles. From Figure 1b, the carbon nanotube has a diameter of 700 nm. The corresponding elemental mappings of the Co-Co_9S_8@SN-CNTs-900 (Figure 1c) clearly exhibit a homogeneous distribution of N, S, O, and Co. Figure 1d and its inset show the amplified FESEM mage and the corresponding EDS line scan. In the scanning across the Co-Co_9S_8@SN-CNTs-900, the C, N, S, O, and Co contents increase on both sides of the nanostructure. These results confirm that the carbon nanotubes exist. As can be seen from the TEM images (Figure 1e), the length of the carbon nanotube consisting of nanoparticles is greater than or equal to 10 μm. From Figure 1f, there are many double-core@shell nanoparticles connected to each other. The inset of Figure 1f indicates that the average nanoparticle size is approximately 33 nm. In addition, the high-resolution TEM (HRTEM) image (Figure 1g) explicitly indicates the existence of core-shell structure. The inset of Figure 1g is a schematic of the structure in which yellow, red, and gray represent cobalt, Co_9S_8, and carbon, respectively. Figures 1h and 1i show HRTEM images of Co-Co_9S_8@SN-CNT-900 and indicate that the d spacing of 0.205 nm corresponds to

the (111) crystalline plane of the metallic Co lattice (Figure 1h) and the d spacing of 0.286 and 0.338 nm index to the (222) crystalline planes of Co_9S_8 and the (002) crystalline planes of carbon (Figure 1i), respectively. The above results indicate that the prepared core-shell structure consists of an inner metallic Co, a Co_9S_8 core, and an outer carbonaceous layer shell; the double-core@shell nanoparticles can hybridize to form 1D nanotubes. That is, the 1D hybrid structure is comprised of Co-Co_9S_8 core-shell nanostructures wrapped by graphitic carbon co-doped with S and N (confirmed by XPS), which is beneficial to creating a synergistic effect of 1D carbon nanotubes with good electrical conductivity and a Co-Co_9S_8 double core@shell nanostructure with high catalytic activity. [33]

Figure 2a shows the XRD patterns. The diffraction peak appears at approximately 26.3° assigned to the graphitic carbon (002) plane (JCPDS Card No. 41-1487). The diffraction peaks at 44.2°, 51.5°, and 75.8° correspond to the (111), (200), and (220) reflection planes of cubic Co (JCPDS Card No.15-0806), respectively. The principal diffraction peaks observed at 29.8°, 47.2 °, and 51.9° are ascribed to the (311), (511) and (440) planes of cubic Co_9S_8 (JCPDS Card No. 65-6801), respectively. Interestingly, it is noteworthy that metallic Co formed in the low-temperature pyrolytic samples (Co@SN-CNTs-700 and Co@SN-CNTs-800). The XRD results indicate that Co-Co_9S_8 coexists at high temperature. Figures 2b and 2c display that the N_2 adsorption-desorption isotherms exhibit type-IV curves; Table 1 gives the data of the surface area, pore volume, and pore diameters of the samples. It is noteworthy that the Co-Co_9S_8@SN-CNTs-900 has a much larger surface area and pore volume than those of the Co@SN-CNTs-800,

Co@SN-CNTs-700, and Co-MOF-600 (Table 1). As shown in Figure 2c and Table 1, the Co-Co_9S_8@SN-CNTs-900 has two types of mesopores centered at 3.1 and 31.1 nm, demonstrating the formation of a bimodal mesoporous structure. Additionally, Figure 2c shows the pore diameters of the Co@SN-CNTs-800 (2.6 and 18.0 nm), Co@SN-CNTs-700 (18.2 nm), and Co-MOF-600 (3.4 and 22.5 nm). The good catalytic performance of the Co-Co_9S_8@SN-CNTs-900 may be ascribed to the abundant catalytic active sites that possess the dominant bimodal mesoporous hybrid structure with higher surface area and larger pore volume. [34,35]

According to Figure 3a, elemental Co, C, S, N, and O appear in the Co-Co_9S_8@SN-CNTs-900 catalyst, with atomic percentages of 5.6, 78.4, 1.7, 2.8, and 11.5 at.%, respectively. As displayed in Table 2, the doping levels of N and S are easily controlled by simply varying the pyrolytic temperature. In addition, the doping levels of N and S decrease with pyrolytic temperature up to 900 °C, which can lead to increased electrochemical catalytic activity. The Co 2p XPS deconvoluted spectra show six peaks located at 778.3, 781.0, 782.1, 785.8, 793.4, 797.0, and 802.5 eV (Figure 3b). The two peaks at 778.3 and 793.4 eV are assigned to Co 2p3/2 and Co 2p1/2 of metallic Co, respectively. [36-38] The two peaks at 781.0 and 797.0 eV, as well as their satellite peaks at 785.8 and 802.5 eV, are attributed to Co(II) or Co(III) of Co_xS_y. [36-39] The peak at 782.1 eV is ascribed to the Co and N in the form of Co-N_x.

Significantly, the electrocatalytic performance of the catalysts was greatly boosted by the presence of Co-N_x in graphene. [40] As seen from Figure 3c, the C 1s high-resolution spectrum can be divided into three peaks at 285.8, 284.9, and 284.6 eV, which correspond to C-N, C-S, and C=C-C bonds, respectively. [41] The S 2p XPS spectra (Figure 3d) of the pyrolytic catalyst can be divided into five different peaks. The peak at 162.0 eV is due to the C-Co-S bond,

indicating the formation of Co_9S_8 in the sample by pyrolysis.[42] The binding energies of 168.5 and 163.5 eV confirm the formation of C-S-C and C-SO_x-C sulfide, respectively.[43] The binding energies of 161.4 and 162.5 eV are attributed to S 2p3/2 and S 2p1/2, respectively. These results are in accordance with those from the XRD analysis. The presence of C-S and C-N verifies that carbon was co-doped with S and N, which can improve the electrocatalytic performance of the catalyst.[14,42,43] The results further confirm the formation of the hybrid structure and composition. The N 1s XPS spectrum (Figure 3e) of Co-Co_9S_8@SN-CNT-900 confirms three peaks at 398.0, 398.8, and 401.1 eV, revealing the existence of pyridinic-N, Co-N_x, and graphitic-N, respectively. It has been widely accepted that these three kinds of N are three active forms that enhance electrocatalytic performance.[44] The O 1s spectrum (Figure 3f) exhibits three peaks at 530.7, 532.1, and 533.5 eV for C=O, C-OH, and C-O, respectively.[45]

2.3 ORR electrocatalytic performance test

N- and/or S-doped carbon materials have often exhibited superior electrocatalytic activity for ORR. Electrochemical tests reveal that the Co-Co_9S_8@SN-CNTs-900 has superior catalytic performance in the same alkaline electrolyte. The ORR electrocatalytic property tests were first conducted in 0.1-M potassium hydroxide aqueous electrolyte solution saturated with N_2 or O_2 gas using cyclic voltammetry. In Figure 4a, it is clear that an obvious cathodic peak can be observed at 0.81 V for ORR in the O_2 saturated electrolyte, while there are no significant peaks, except for the current capacitive background curves in the N_2 saturated electrolyte solution, indicating that the Co-Co_9S_8@SN-CNTs-900 exhibits excellent ORR performance.

To gain deeper insights into ORR activity with the Co-Co_9S_8@SN-CNTs-900, RDE measurements were recorded at a scan rate of 5 mV s^{-1} in O_2 saturated 0.1-M potassium

hydroxide aqueous electrolyte solution. Compared with the Co-MOF-600, Co@SN-CNTs-700, and Co@SN-CNTs-800, the Co-Co_9S_8@SN-CNTs-900 shows the highest electrocatalytic performance in the ORR, with an onset potential of up to 0.90 V and a half-wave potential of 0.81 V (Figure 4b). The limiting current density of the Co-Co_9S_8@SN-CNTs-900 is greater than that of Pt/C, despite the ORR onset potential and half-wave potential being less than those of Pt/C (0.98 and 0.84 V versus RHE). Those values are comparable to some reported Co-based catalysts toward ORR, such as HP-CoNCNFs (0.85 V *vs.* RHE and 2.3 mA cm^{-2}) [46] and Co-NSCNTs (0.87 V *vs.* RHE and 4.5 mA cm^{-2}) [47].These results suggest that the Co-Co_9S_8@SN-CNTs-900 has better ORR performance. Figure 4c displays the polarization curves of the Co-Co_9S_8@SN-CNTs-900 under rotation speeds varying from 400 to 1600 rpm. Increasing rotation speed led to higher limiting current density, which can be attributed to the shortened diffusion distance at fast speeds.[48] The Koutecky−Levich plots are presented in Figure 4d. It is apparent that the Co-Co_9S_8@SN-CNTs-900 displayed a good linearity and near-parallel properties in all the plots at various potentials between 0.7 and 0.4 V versus RHE. This result implies first-order reaction kinetics toward the concentration of dissolved oxygen. The average electron-transfer number is close to 4.0, indicating that the ORR (0.4−0.7 V versus RHE) is a four-electron process.

2.4 OER electrocatalytic performance test

In order to demonstrate the potential application of the Co-Co_9S_8@SN-CNTs-900 as a tri-functional catalyst, the OER activity of the Co-MOF-600, Co@SN-CNTs-700, Co@SN-CNTs-800, and Co-Co_9S_8@SN-CNTs-900, as well as the OER polarization curve measurements of

commercial Ir/C catalysts, underwent further investigation. Figure 5a shows that the Co-Co_9S_8@SN-CNTs-900 exhibits the best activity among the five catalysts, having the largest limiting current density and the smallest onset potential (35.2 mA cm^{-2} and 1.48 V versus RHE). The other four catalysts are Co-MOF-600 (26.3 mA cm^{-2} and 1.52 V versus RHE), Co@SN-CNTs-700 (30.5 mA cm^{-2} and 1.51 V versus RHE), Co@SN-CNTs-800 (32.1 mA cm^{-2} and 1.50 V versus RHE), and commercial Ir/C (30 mA cm^{-2} and 1.46 V versus RHE). The OER onset potential of the Co-Co_9S_8@SN-CNTs-900 is also comparable to some reported non-precious metal catalysts, such as SHG (1.49 V *vs.* RHE)[49] and $FeNiS_2$ (1.45 V *vs.* RHE) [50]. Tafel slope is a significant measure in evaluating OER activity, and describes the influence of overpotential on steady-state current density.[51] As shown in Figure 5b, the Tafel slope of the Co-Co_9S_8@SN-CNTs-900 catalyst (94 mV dec^{-1}) is close to that for Ir/C (96 mV dec^{-1}). The Tafel slopes of the other three catalysts are 167, 122, and 118 mV dec^{-1} for Co-MOF-600, Co@SN-CNTs-700, and Co@SN-CNTs-800, respectively. Hence, the Co-Co_9S_8@SN-CNTs-900 catalyst demonstrates faster OER kinetics. In general, the Co-Co_9S_8@SN-CNTs-900 catalyst has a higher OER performance than traditional noble-metal catalysts.

EIS measurements were performed to analyze the electrode kinetics and impedance of the Co-Co_9S_8@SN-CNTs-900 catalyst. The Nyquist plots of the Co-MOF-600, Co@SN-CNTs-700, Co@SN-CNTs-800, Co-Co_9S_8@SN-CNTs-900, and commercial Ir/C catalysts (Figure 5c) display depressed semicircles on the whole, with the Co-Co_9S_8@SN-CNT-900 catalysts

displaying the smallest diameters. According to the Nyquist plots, the charge-transfer resistance (Rct) of the Co-Co_9S_8@SN-CNTs-900 catalysts is 28.6 Ω, while the Rct values for Co-MOF-600, Co@SN-CNTs-700, Co@SN-CNTs-800, and commercial Ir/C are 80, 47, 46, and 30 Ω, respectively. The Rct values for Co-MOF-600, Co@SN-CNTs-700, Co@SN-CNTs-800, Co-Co_9S_8@SN-CNTs-900, and commercial Ir/C are 50, 34, 33, 18, and 20 Ω, respectively. Porous structure with the more catalytic active sites and higher surface area can promote OER-related mass transport. The above results further confirm that the Co-Co_9S_8@SN-CNTs-900 catalyst possesses a faster OER reaction rate than the other four catalysts in this experiment.

2.5 HER electrocatalytic performance test

The HER activity of the Co-Co_9S_8@SN-CNT-900 was also evaluated using the three-electrode electrochemical configuration. For comparison, the activity of Co-MOF-600, Co@SN-CNTs-700, Co@SN-CNTs-800, and commercial Pt/C was also investigated under the same conditions. As shown in Figure 6a and 6b, the Co-Co_9S_8@SN-CNTs-900 also exhibit superior HER performance, a smaller onset potential (-0.12 V versus RHE), and a smaller Tafel slope (92 mV dec^{-1}). The HER onset potential and Tafel slope of the other four catalysts are -0.15 V versus RHE and 159 mV dec^{-1}, -0.14 V versus RHE and 129 mV dec^{-1}, and -0.14V versus RHE and 128 mV dec^{-1} for Co-MOF-600, Co@SN-CNTs-700, and Co@SN-CNTs-800, respectively, indicating that the HER activity improves with increasing pyrolysis temperature. Moreover, the

values for Co-Co_9S_8@SN-CNTs-900 are also comparable to the behavior of some non-precious-metal-based catalysts, such as Co-NRCNTs (−0.24 V versus RHE) [52] and $NiCo_2S_4$ (−0.17 V versus RHE)[53], suggesting the outstanding HER activity of the Co-Co_9S_8@SN-CNT-900.

2.6 Stability test

The stability tests of the Co-Co_9S_8@SN-CNTs-900 and the commercial Pt/C and Ir/C catalysts were performed in potassium hydroxide aqueous solution. The results indicate that the negative shift of the half-wave potential (19 mV) for the Co-Co_9S_8@SN-CNTs-900 is lower than that of the Pt/C catalysts (46 mV) after 5000 cycles (Figure 7a). Furthermore, the limiting current densities of the Co-Co_9S_8@SN-CNTs-900 display no significant change before and after 5000 cycles, while the limiting current densities of the Pt/C catalysts decreased by 0.31 mA cm^{-2}.

The results of galvanostatic experiments (Figure 7b) indicate that the Co-Co_9S_8@SN-CNTs-900 can continuously produce oxygen for more than 10 h without changing the recorded overpotentials at current density of 10 mA cm^{-2} compared to commercial Ir/C catalysts. In addition, the HER stability tests of the Co-Co_9S_8@SN-CNTs-900 and Pt/C catalysts (Figure 7c) were performed to study their electrochemical performance. The Co-Co_9S_8@SN-CNTs-900 decreases slightly in current density to 15.4 mA cm^{-2}, whereas the Pt/C decreases to 24.1 mA cm^{-2}. The negative overpotential shift of the Co-Co_9S_8@SN-CNTs-900 is 14 mV (10 mA cm^{-2}, before and after 200 cycles), whereas for the Pt/C it is 32 mV. These detailed results indicate that the Co-Co_9S_8@SN-CNTs-900 exhibits superior catalytic performance in ORR, OER, and HER,

as well as exhibiting better stabilities compared with commercial Pt/C and Ir/C catalysts, due to its special composition and structure.

2.7 Overall water splitting

In order to demonstrate that Co-Co_9S_8@SN-CNTs-900 is an efficient trifunctional electrocatalyst, we fabricated a two-electrode system in which the Co-Co_9S_8@SN-CNTs-900 is used as both a cathode and anode in 0.1-M potassium hydroxide aqueous electrolyte solution for electrochemical water splitting. Figure S1a (see Supplementary Information) indicates that the potential of Co-Co_9S_8@SN-CNTs-900 (1.49 V) is superior to that of CoP-MNA (1.62 V), as well as that of the cobalt sulfide/carbon nanotube (1.74 V) at 10 mA cm^{-2}.[54, 55] Obvious H_2 and O_2 bubbles are generated on the electrodes; see the inset of Figure S1a. The stability of the electrolyzer is a crucial criterion in the evaluation of electrolyzer systems. Therefore, a test of the electrolyzer's durability was conducted at 1.49 V in 0.1M potassium hydroxide aqueous solution for approximately 15 h (Figure S1b), and it was found to remain stable for nearly the entire 15 h, exhibiting only a slight decrease in current density during the first hour. These results demonstrate that Co-Co_9S_8@SN-CNTs-900 can be used as a promising catalyst in commercial water splitting.

2.8 Zinc-air battery tests

Finally, a practical single-cell zinc air battery (ZnAB) was assembled by employing Co-Co_9S_8@SN-CNTs-900 catalyst as the active air electrode material and O_2 in the air as the oxidant to explore the feasibility of the Co-Co_9S_8@SN-CNTs-900 for future practical applications. Figure S2a displays the polarization curves of the rechargeable ZnABs during the battery

charging-discharging process with the Co-Co_9S_8@SN-CNTs-900 catalyst, Pt/C, and Ir/C catalysts used as air electrodes separately. The Co-Co_9S_8@SN-CNTs-900 catalyst shows smaller overpotentials relative to Pt/C+Ir/C both in the charging and discharging processes. The maximum power density of the Co-Co_9S_8@SN-CNTs-900 catalyst (93 mW cm^{-2}) is prominently larger compared to the Pt/C and Ir/C catalysts (59 mW cm^{-2}) (Figure S2b). The single-cell ZnAB performance of the Co-Co_9S_8@SN-CNTs-900, Pt/C, and Ir/C catalysts are displayed in Figure S2c. The Co-Co_9S_8@SN-CNTs-900 catalyst reveals an initial discharge potential of 1.1 V versus RHE and charge potential of 2.1 V. The two values remain stable after 90 h, indicating that the Co-Co_9S_8@SN-CNTs-900 catalyst applied in the rechargeable ZnABs demonstrates outstanding cycling stability.

3. Conclusion

In summary, 1D Co-Co_9S_8@SN-CNTs-900 obtained by pyrolysis of the Co-MOFs displayed excellent ORR, OER, and HER multifunctional catalytic activity. Furthermore, it displayed good performance and excellent stability for more than 15 h used as both an anode and cathode catalyst in an alkaline water electrolyzer. In addition, it also exhibited superior catalytic performance and cycling stability compared with Pt/C and Ir/C integrated into a rechargeable ZnAB. The outstanding performance could be ascribed to the special hybrid porous tubular nanostructure consisting of core-shell nanoparticles with a Co-Co_9S_8 core and graphitic carbon co-doped with S and N, the combination of which possesses the advantageous features of both 1D nanostructures and core-shell nanostructures. Our research also shows that electrocatalytic performance is mainly dependent on the doping level of heteroatoms and the morphology of

catalysts, which are controlled by varying the calcination temperature. In this paper, we presents a new and simple method for fabricating carbon-based composite materials embedded with cobalt and Co_9S_8 and co-doped with S and N without additional S and N sources using Co-MOF precursors for electrocatalysis.

4. Materials and methods

4.1 Synthesis of Co-MOFs

In a typical synthesis procedure for Co-MOFs, 291 mg of $Co(NO_3)_2.6H_2O$ was dissolved in a mixed solvent of 10 ml of dimethylformamide (DMF) and 10 ml of deionized water. Then, 156 mg of Bpy (4,4'-bipyridine) and 172 mg of Tdc (thiophene-2,5-dicarboxylate) were slowly added to the solvent with vigorous stirring. After reaction for 60 min at ambient temperature, the solution was transferred to a 30 ml autoclave and kept at 105 °C for 3 d. The resulting light pink powder was gained, filtrated, and washed with ample ethanol and dried under vacuum at 40°C overnight. The product weighed 0.316 g and was denoted Co-MOFs.

4.2 Synthesis of Co-Co_9S_8@SN-CNTs

The above-prepared 500-mg precursor was transferred to a quartz boat in a tubular furnace, which was flushed with Ar for 45 min. The furnace was heated to different temperatures (600ºC, 700ºC, 800ºC, and 900 ºC) for 180 min under Ar atmosphere at a heating rate of 3ºC/min. The correspondingly obtained porous products were named Co-MOF-600, Co@SN-CNTs-700, Co@SN-CNTs-800, and Co-Co_9S_8@SN-CNTs-900, respectively.

4.3 Characterization

X-Ray-diffraction data were recorded on an X-ray diffractometer (Bruker D8 Advance, Germany) using Cu Kα radiation (λ=0.15406 nm) to confirm the samples' identities and phases. The samples were observed by transmission electron microscopy (TEM) using a JEM-2100 electron microscope and by field-emission scanning electron microscopy (FE-SEM) using a SUPRA40 instrument to further analyze the morphology and microstructures of the samples. The surface chemical species of the Co-Co_9S_8@SN-CNTs-900 were determined by X-ray photoelectron spectroscopy (XPS) using a VG ESCALAB 220I-XL system (Thermo Scientific, USA). N_2 adsorption-desorption isotherm measurements at 77 K were carried on an ASAP 2020 apparatus (Micromeritics, Inc., USA). The specific surface areas and the porosity of the catalysts were studied by the Brunauer-Emmet-Teller (BET) method.

4.4 Electrochemical measurements

ElectrElectrochemical tests were carried out in a three-electrode electrochemical workstation (CHI660D, ChenHua Instruments, Shanghai, China), which consisted of a working electrode (glassy carbon rotating disk electrode, RDE, 0.1256 cm^2), a counter electrode (Pt foil, 1 cm$\times$1 cm), and a reference electrode (saturated calomel electrode). A graphite rod was used as the counter electrode for HER only. All measured potentials were converted to values with reference to a reversible hydrogen electrode (RHE) reference scale. During the testing process, a gas-flow system was used to ensure gas saturation of the electrode. Prior to use, the RDE surface was initially polished with alumina slurry, followed by ultrasonic cleaning in ethanol and deionized water

successively. Four (4) milligrams of the catalyst were dispersed in 970 μL of absolute ethanol mixed solvent with 30 μL of 5-wt.% Nafion solution and then ultrasonicated for at least 30 min until it became a homogeneous ink. Then, 12.8 μL of the dispersion was coated onto the RDE electrode (4 mm in diameter) and dried using an infrared light. The catalyst and commercial Pt/C (20%) catalyst loadings were both 400 μg cm^{-2}.

OER, HER, and ORR tests were carried out in an O^{2-} or N^{2-}saturated 0.1M potassium hydroxide aqueous electrolyte by bubbling oxygen or nitrogen gas for 3 h prior to measurements. The polarization data were obtained in the above solution with the potential varied in the ranges between 1.2 and 0 V, 1 and 1.86 V, and 0 and −0.6 V versus the RHE at 5-mV intervals. OER and HER tests were measured at a rotation speed of 900 rpm. The Nyquist plots were measured in the potential at 1.58 V versus the RHE. The spectra were scanned in a frequency range from 105 to 10^{-2} Hz and at an AC amplitude of 5 mV at room temperature. ORR tests were measured at rotation speeds of 400, 625, 900, 1225, and 1600 rpm at 25°C±1°C.

4.5 Air electrode preparation

To prepare a Zn-air battery, catalysts were dispersed into the Nafion ionomer (5 wt.% solution) and ethanol to form the catalyst ink. Then, the catalyst ink was spray-coated on top of the gas diffusion layer (Ion Power Inc., 25 BC). The loading of the catalyst was 0.8 mg cm^{-2}. The zinc electrode was prepared using a zinc foil with an exposed area of 2 cm^{-2} and the electrolyte solution was a 6.0-M potassium hydroxide aqueous solution. Galvanostatic discharge and charge-cycling measurements were carried out at 5 mA cm^{-2}

using a recurrent galvanic pulse method with each charge-discharge step being held for 20 min.

Acknowledgements

This work was supported by the National Natural Science Foundation of China (Grant No. 21571053), the Program for Innovative Research Team in Science and Technology (Grant No. 16IRTSTHN004) of the University of Henan Province, and by the 111 Project (No. D17007). We would like to thank LetPub (www.letpub.com) for providing linguistic assistance during the preparation of this manuscript. J. Lu gratefully acknowledges support from the U. S. Department of Energy (DOE), Office of Energy Efficiency and Renewable Energy, Vehicle Technologies Office. Argonne National Laboratory is operated for DOE Office of Science by UChicago Argonne, LLC, under contract number DE-AC02-06CH11357.

Appendix A. Supplementary material

Supplementary data associated with this article can be found in the online version.

Conflict of Interest

The authors declare no conflict of interest.

References

[1] X. Chen, B. Liu, C. Zhong, Z. Liu, J. Liu, L. Ma, Y. Deng, X. Han, T. Wu, W. Hu and J. Lu, *Advanced Energy Materials*, 2017, **7**, 1700779.

[2] Y. Jiao, Y. Zheng, M. Jaroniec and S. Z. Qiao, *Chem. Soc. Rev.*, 2015, **44**, 2060-2086.

[3] X. Chen, C. Zhong, B. Liu, Z. Liu, X. Bi, N. Zhao, X. Han, Y. Deng, J. Lu and W. Hu, Small, 2018, DOI: 10.1002/smll.201702987.

[4] Y. Li, C. Zhong, J. Liu, X. Zeng, S. Qu, X. Han, Y. Deng, W. Hu and J. Lu, *Adv. Mater.*, 2018, **30**, 1703657.

[5] J. K. He, M. C. Wang, W. B. Wang, R. Miao, Z. W. Chen, S. Y. S. Poges, T. Jafari, W. Q. Song, J. C. Liu and S. l. Suib, *ACS Appl. Mater. Interfaces*, 2017, **9**, 42676-42687.

[6] H. F. Lv, D. G. Li, D. S. Strmcnik, A. P. Paulikas, N. M. Markovic and V. R. Stamenkovic, *Nano energy*, 2016, **29**, 149-165.

[7] C. C. L. Mccrory, S. H. Jung, I. M. Ferrer, S. M. Chatman, J. C. Peters and T. F. Jaramillo, *J. Am. Chem. Soc.*, 2015, **137**, 4347-4357.

[8] X. Han, X. Wu, Y. Deng, J. Liu, J. Lu, C. Zhong and W. Hu, *Advanced Energy Materials*, 2018, **1800935**.

[9] F. L.Yang, P. P. Zhao, X. Hua, W. Luo, G. Z. Cheng, W. Xing and S. L. Chen, *J. Mater. Chem. A*, 2016, **41**, 16057-16063.

[10] D. W. Wang and D. S. Su, *Energy Environ. Sci.*, 2014, **7**, 576-591.

[11] Z. H. Sheng, L. Shao, J. J. Chen, W. J. Bao, F. B. Wang and X. H. Xia, *ACS Nano.*, 2011, **5**, 4350-4358.

[12] S. B. Yang, L. J. Zhi, K. Tang, X. L. Feng, J. Maier and K. MÜllen, *Adv. Funct. Mater.* 2012, **22**, 3634-3640.

[13] Z. W. Liu, F. Peng, H. J. Wang, H. Yu, W. X. Zheng and J. Yang,, *Angew. Chem., Int. Ed.*, 2011, **50**, 3257-3261.

[14] L. J. Yang, S. J. Jiang, Y. Zhao, L. Zhu, S. Chen, X. Z. Wang, Q. Wu, J. Ma, Y. W. Ma and Z. Hu, *Angew. Chem., Int. Ed.*, 2011, **50**, 7132-7135.

[15] Y. B. Li, H. M. Zhang, Y. Wang, P. R. Liu, H. GYang, X. D. Yao, D. Wang, Z. Y. Tang and H. J. Zhao, *Energy Environ. Sci.*, 2014, **7**, 3720-3726.

[16] A. Sivanantham, P. Ganesan and S. Shanmugam, *Adv. Funct. Mater.*, 2016, **26**, 4660-4660.

[17] M. Shen, C. Ruan, Y. Chen, C. Jiang, K. Ai and L. Lu, *Acs Appl. Mater. Interfaces*, 2015, **7**, 1207-1218.

[18] Y. X. Zhou, H. B. Yao, Y. Wang,H. L. Liu, M. R. Gao, P.K. Shen and S. H. Yu, *Chem. Eur. J.*, 2010, **16**, 12000-12007.

[19] R. A. Sidik and A. B. Anderson, J. Phys. Chem. B, 2006, **110**, 936-941.

[20] H. Wang, Y. Liang, Y. Li and H. Dai, *Angew. Chem. Int. Ed.*, 2011, **50**, 10969-10972.

[21] N. A. Vante and H. Tributsch, *Nature*, 1986, **323**, 431-432.

[22] Y. X. Zhou, H. B. Yao, Y. Wang, H. L. Liu, M. R. Gao, P. K. Shen and S. H. Yu, *Chem. Eur. J.*, 2010, **16**, 12000-12007.

[23] Y. J. Feng, T. He and N. Alonso-Vante, *Chem. Mater.*, 2008, **20**, 26-28.

[24] M. R. Gao, Q. Gao, J. Jiang, C. H. Cui, W. T. Yao and S. H. Yu, *Angew. Chem. Int. Ed.*, 2011, **50**, 4905-4908.

[25] Q. Li, R. Cao, J. Cho and G. Wu, *Adv. Energy Mater.*, 2014, **4**, n/a-n/a.

[26] Z. H. Wen, S. Q. Ci, F. Zhang, X. L. Feng, S. M. Cui, S. Mao, S. L. Luo, Z. He and L. H.Chen, *Adv. Mater.*, 2012, 24, 1399-1404.

[27] R. A. Sidik, A. B. Anderson, N. P. Subramanian, S. P. Kumaraguru and B. N. Popov, *J. Phys. Chem. B*, 2006, **110**, 1787-1793.

[28] L. P. Zhang, and Z. H. Xia, *J. Phys. Chem. C*, 2011, **115**, 11170-11176.

[29] K. P. Gong, F. Du, Z. H. Xia, M. Durstock, L. M. Dai, *Science*, 2009, **323**, 760-764.

[30] F. L. Yang, P. P. Zhao, X. Hua, W. Luo, G. Cheng, Z. W. Xing and S. L. Chen, *J. Mater. Chem. A*, 2016, **4**, 16057-16063.

[31] Z. J. Wang, Y. Z. Lu, Y. Yan, T. Y. P. Larissa, X. Zhang, D. Wuu, H. Zhang, Y. H. Yang, X. Wang, *Nano Energy*, 2016, **30**, 368-378.

[32] T. Wu, M. Y. L.; Pi, X. D. Wang, D. K. Zhang and S. Chen, *J. Phys. Chem. Chem. Phys.*, 2017, **19**, 2104-2110.

[33] Q. L. Wei, F. Y. Xiong, S. S. Tan, L. Huang, E. H. Lan, B. Dunn, and L. Q. Mai, *Adv. Mater.*, 2017, **29**, 1602300.

[34] Y. Tang, F. Jing, Z. Xu, F. Zhang, Y. Mai and D. Wu, *ACS Appl. Mater. Inter.*, 2017, **14**, 12340-12347.

[35] S. Liu, M. Tong, G. Liu, X. Zhang, Z. Wang, G. Wang, W. Cai, H. Zhang and H. Zhao, *Inorg. Chem. Front.*, 2017, **4**, 491-498.

[36] X. Zhang, S. W. Liu, Y. P. Zang, R. R. Liu, G. Q. Liu, G. Z. Wang, Y. X. Zhang, H. M. Zhang and H. J. Zhao, *Nano Energy*, 2016, **30**, 93-102.

[37] X. Zhang, K. Y. Tsang, and K. Y. Chan, *J. Electroanal. Chem.*, 2004, **573**, 1-9.

[38] H. Y. Jin, J. Wang, D. F. Su, Z. Z. Wei, Z. F. Pang, and Y. Wang, *J. Am. Chem. Soc.*, 2015, **137**, 2688-2694.

[39] X. Zhang, R. Liu, Y. Zang, G. Liu, G. Wang, Y. Zhang, H. Zhang and H. Zhao, *Chem. Commun.*, 2016, **52**, 5946-5949.

[40] H. C. Huang, I. Shown, S. T. Chang, H. C. Hsu, H. Y. Du, M. C. Kuo, K. T. Wong, S. F. Wang, C. H. Wang, L. C. Chen, and K. H. Chen, *Adv. Funct. Mater.*, 2012, **16**, 3500-3508.

[41] M. Wang, J. R. Huang, M. Wang, D. E. Zhang, W. M. Zhang, W. H. Li and J. Chen, *Electro. Commu.*, 2013, **34**, 299-303.

[42] L. L. Feng, G. D. Li, Y. P. Liu, Y. Y. Wu, H. Chen, Y. Wang, Y. C. Zou, D. J. Wang and X. X. Zou, *ACS Appl. Mater. Interface*, 2015, **7**, 980-988.

[43] X. C. Cao, X. J. Zheng, J. H. Tian, C. Jin, K. Ke and R. Z. Yang, *Electrochimica Acta*, 2016, **191**, 776-783.

[44] S. J. Chao, Q. Cui, K. Wang, Z. Y. Bai, L. Yang and J. L. Qiao, *J. Power Sources*, 2015, **288**, 128-135.

[45] X. Q. Lin, X. Z. Li, F. Li, Y. Y. Fang, M. Tian, X. C. An, Y. Fu, J. Jin and J. T. Ma, *J. Mater. Chem. A*, 2016, **17**, 6505-6512.

[46] S. G. Wang, Z. T. Cui and M. H. Cao, *Chem. Eur. J.*, 2015, **21**, 2165-2172.

[47] S. W. Liu, X. Zhang, G. Z. Wang and Y. X. Zhang, *ACS Applied Materials & Interfaces*, 2017, **39**, 34269-34278.

[48] G. P. Kim, H. H. Sun and A. Manthiram, *Nano Energy*, 2016, **30**, 130-137.

[49] C.G. Hu and L.M. Dai, *Adv. Mater.*, 2017, **29**, 1604942.

[50] J. Jiang, S. Lu, H. Gao, X. Zhang and H.Q. Yu, *Nano Energy*, 2016, **27**, 526-534.

[51] S. Mao, Z. Wen, T. Huang, Y. Hou and J. Chen, *Energy Environ. Sci.*, 2014, **7**, 609-616.

[52] X. Zou, X. Huang, A.Goswami, R. Silva, B. R. Sathe, E. Mikmekova and T. Asefa, *Angew. Chem., Int. Ed.*, 2014, **53**, 4372-4376.

[53] Y. Y. Wu, G. D. Li, Y. P. Liu, L. Yang, X. R. Lian, T. Asefa and X. X. Zou, *Adv. Funct. Mater.*, 2016, **26**, 4839-4847.

[54] *Y. P. Zhu, Y. P. Liu, T. Z. Ren and Z. Y. Yuan, Adv. Funct. Mater.*, 2015, **25**, 7337-7347.

[55] J. Wang, H. X. Zhong, Z. L. Wang, F. L. Meng, X. B. Zhang, *ACS Nano*, 2016, **10**, 2342-2348.

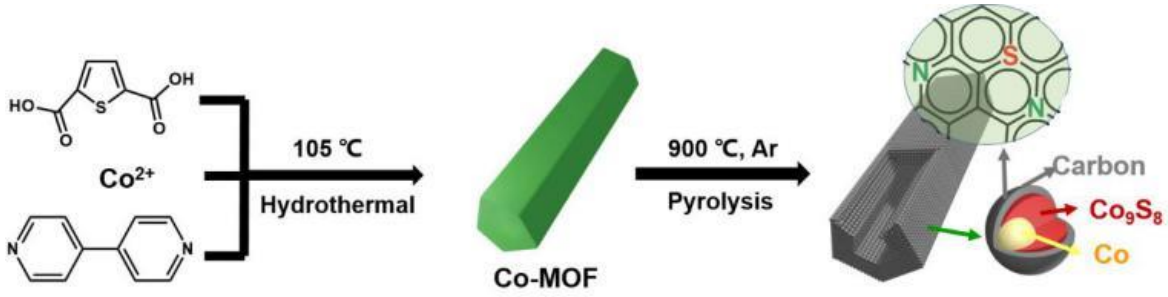

Scheme 1. Formation process of the Co-Co_9S_8@SN-CNTs-900 catalyst.

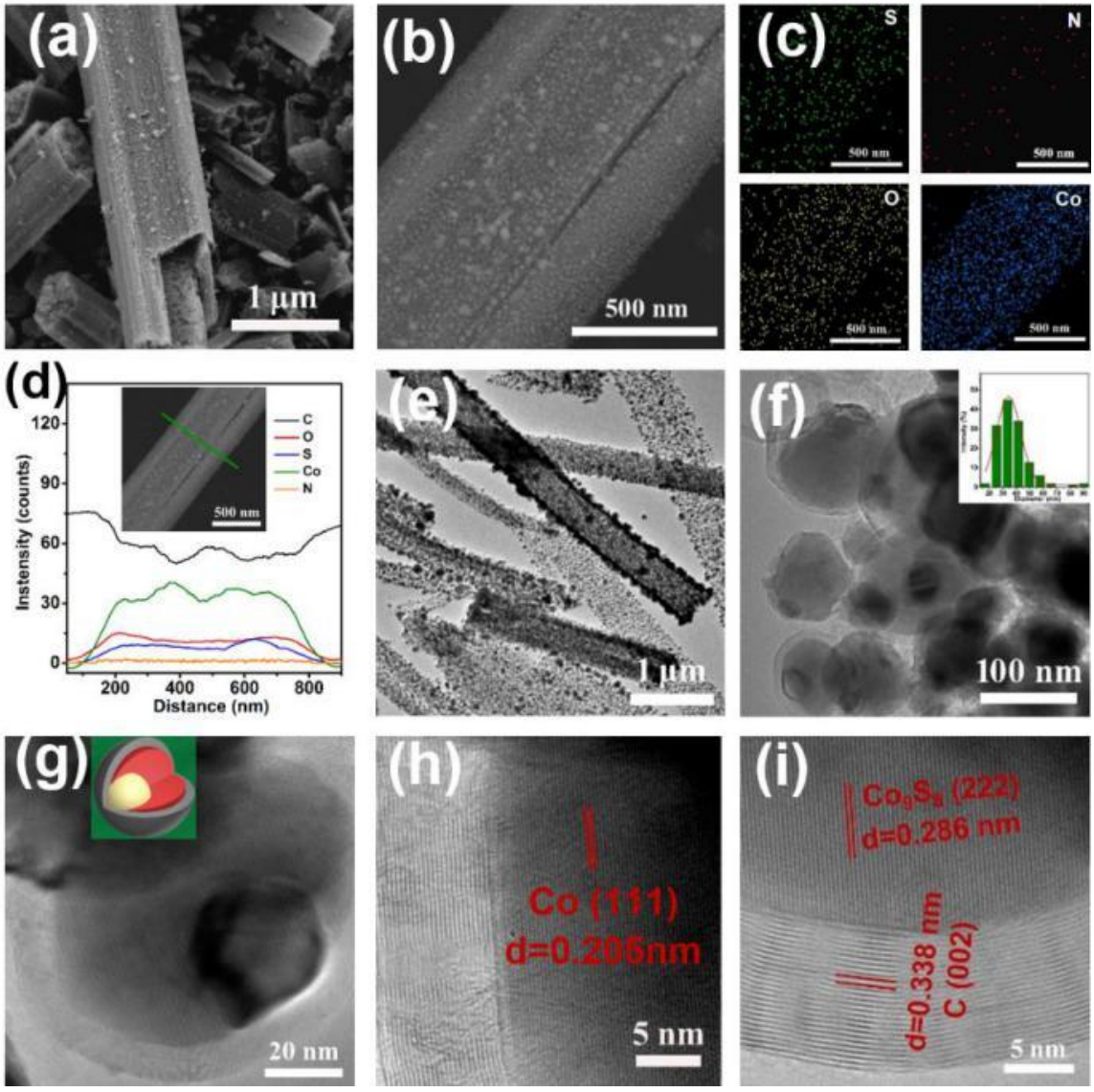

Figure 1. (a and b) FESEM images; (c) the corresponding elemental mappings; (d) EDS line scan (inset is corresponding FESEM images); (e and f) TEM images (inset is

corresponding size distribution); (g-i) HRTEM images of the Co-Co_9S_8@SN-CNT-900 catalyst.

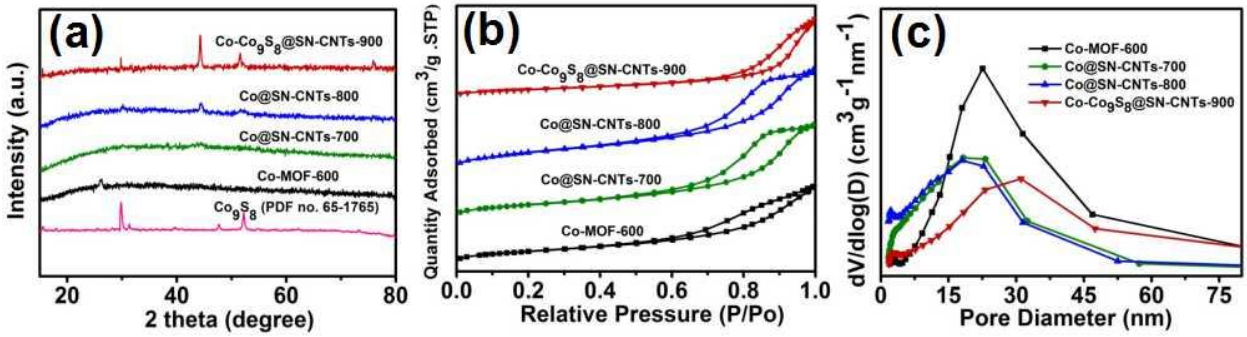

Figure 2. (a) XRD patterns, (b) N_2 adsorption-desorption isotherms, and (c) corresponding pore size distribution curves of Co-MOF-600,Co@SN-CNTs-700, Co@SN-CNTs-800, and Co-Co_9S_8@SN-CNTs-900.

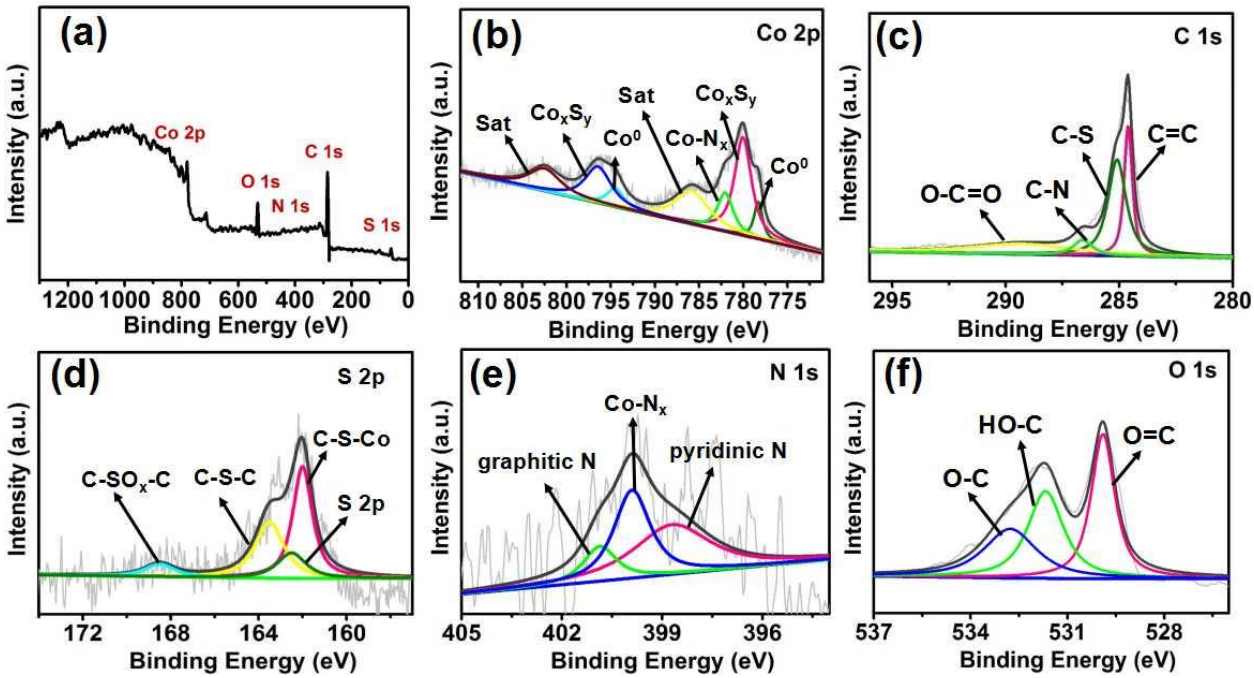

Figure 3. (a) XPS full spectrum, and high-resolution spectra for (b) Co 2p, (c) C 1s, (d) S 2p, (d) N 1s, and (e) O 1s for Co-Co_9S_8@SN-CNTs-900.

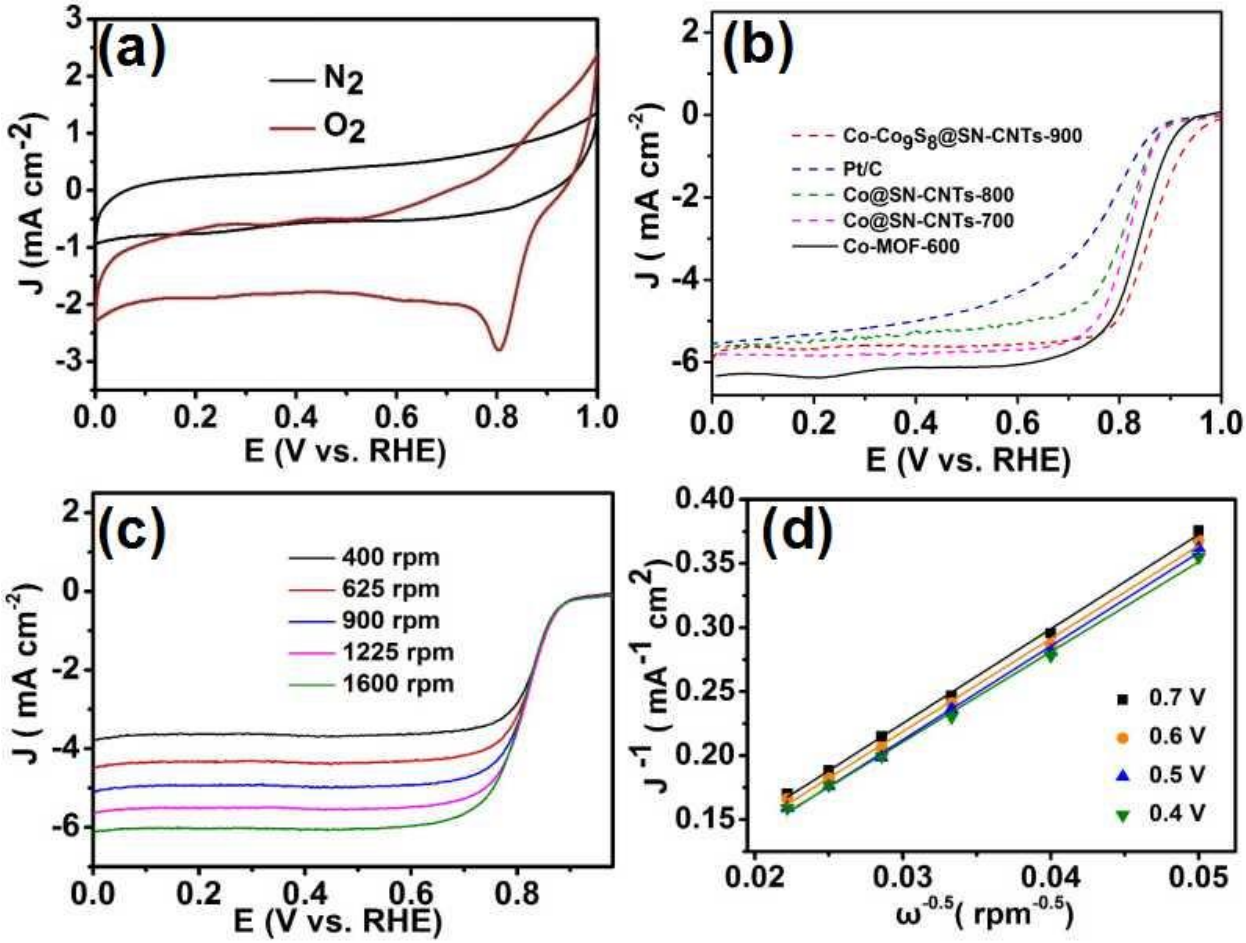

Figure 4. (a) CV curves of the Co-Co_9S_8@SN-CNTs-900 catalyst in O_2 and N_2 saturated 0.1 M KOH electrolyte solution; (b) polarization curves of the Co-MOF-600, Co@SN-CNTs-700, Co@SN-CNTs-800, Co-Co_9S_8@SN-CNTs-900, and Pt/C catalysts at 1600 rpm; (c) polarization curves of the Co-Co_9S_8@SN-CNTs-900 with different rotation rates; (d) Koutecky-Levich plots of the Co-Co_9S_8@SN-CNTs-900 catalyst at 0.7, 0.6, 0.5 and 0.4 V vs. RHE.

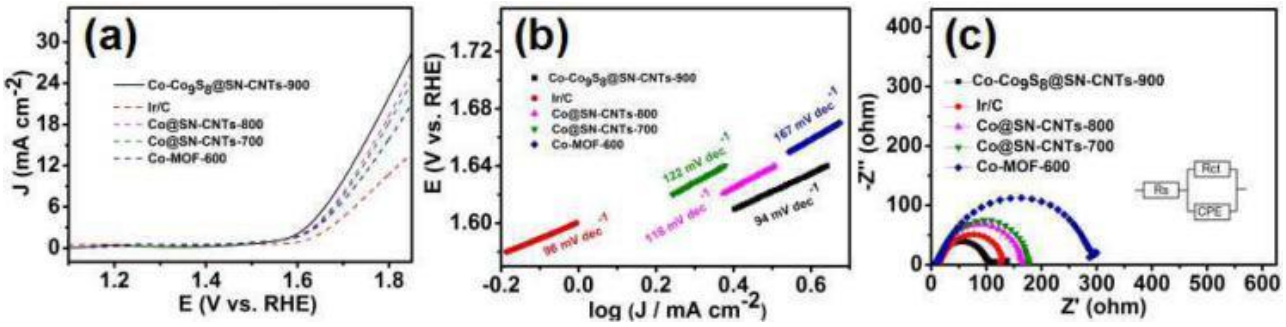

Figure 5. (a) Polarization curves for the OER of the Co-MOF-600, Co@SN-CNTs-700, Co@SN-CNTs-800, Ir/C and Co-Co_9S_8@SN-CNTs-900 catalysts in N_2-saturated 0.1-MKOH at 5 mV s^{-1} and 900 rpm. (b) Tafel plots of the five catalysts derived from (a). (c) Nyquist plots (a potential of 1.60 V vs. the RHE) of the five catalysts.

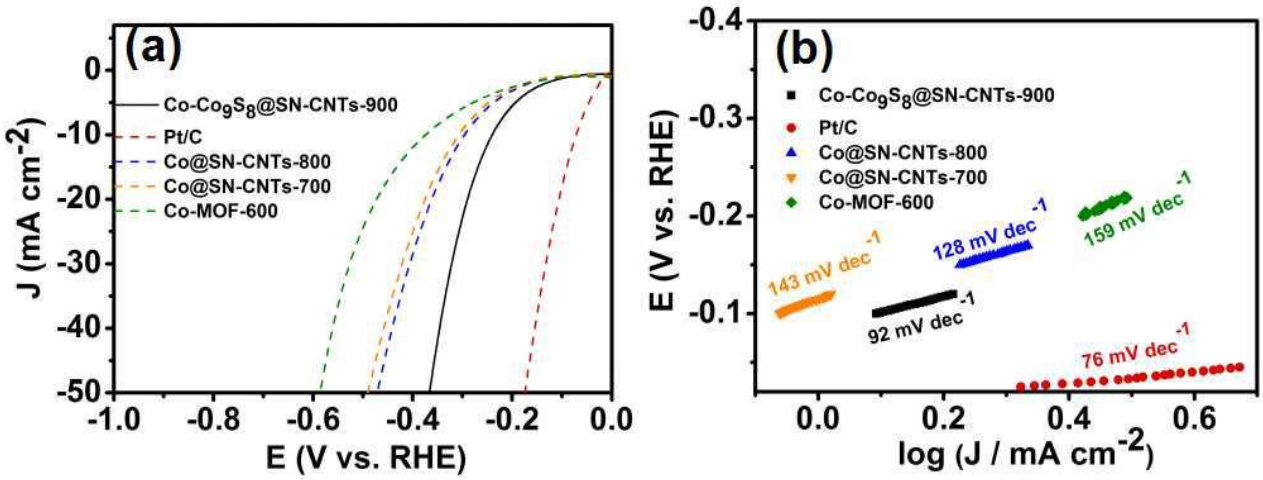

Figure 6. (a) HER polarization curves of the Co-MOF-600, Co@SN-CNTs-700, Co@SN-CNTs-800, and Co-Co_9S_8@SN-CNTs-900 catalysts at 5 mV s^{-1} at 900 rpm in N_2 saturated 0.1 M KOH solution. (b) Corresponding Tafel plots of the Co-MOF-600, Co@SN-CNTs-700, Co@SN-CNTs-800, and Co-Co_9S_8@SN-CNTs-900.

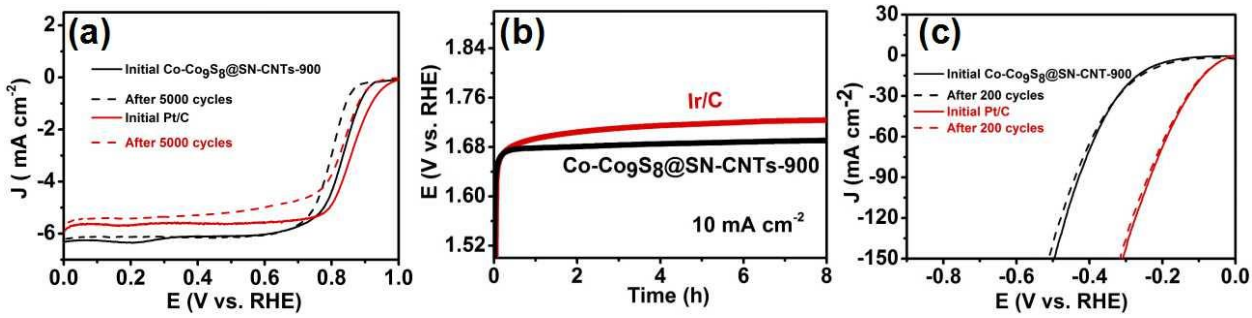

Figure 7. (a) ORR polarization curves of the Co-Co_9S_8@SN-CNTs-900 and Pt/C catalysts in the first and 5000th potential cycles in O_2 saturated 0.1 M KOH (scan rate 50 mV s^{-1}). (b) Chronopotentiaometriy curves of the Co-Co_9S_8@SN-CNTs-900 and commercial Ir/C catalysts at constant current densities of 10 mA cm^{-2} in 0.1 M KOH. (c) HER polarization curves of the Co-Co_9S_8@SN-CNTs-900 and Pt/C in N_2 saturated 0.1 M KOH electrolyte for the first and the 200th potential cycles at 5 mV s^{-1} at 900 rpm. The potential cycles for ORR and HER were from 0 to 1.2 V, and from 0 to −0.6V vs. RHE, at 50 mV s^{-1}.

Sample	Surface area (m^2 g^{-1})	Pore volume (cm^3 g^{-1})	Pore diameters (nm)
Co-MOF-600	141.1	0.44	3.4, 22.5
Co@SN-CNTs-700	240.3	0.46	18.2
Co@SN-CNTs-800	258.3	0.55	2.6, 18.0
Co-Co_9S_8@SN-CNTs-900	345.3	0.60	3.1, 31.1

Table1. Surface area, pore volume, and pore diameters of samples

	C(at. %)	N (at. %)	S (at. %)	O (at. %)	Co(at. %)
Co-MOF-600	44.37	3.89	2.72	32.01	17.01
Co@SN-CNTs-700	64.67	5.18	5.05	11.52	13.58
Co@SN-CNTs-800	74.53	3.51	3.82	12.81	5.97
Co-Co_9S_8@SN-CNTs-900	78.39	2.74	1.65	11.49	5.73

Table 2. Atomic percentages of C, N, S, O, and Co in Co-MOF-600, Co@SN-CNTs-700, Co@SN-CNTs-800, and Co-Co_9S_8@SN-CNTs-900

Personal Portrait Photo and Biosketch

Huijuan Han received her M. S. (2007) and Ph.D. degree (2018) from Henan Normal University, Xinxiang, Henan, P. R. China. She is now a lecturer in Henan Institute of Science and Technology. Her main research interests are the synthesis of MOF-derived-heteroatom-doped porous carbon electrocatalysts for ORR, OER, and HER applications.

Dr. **Zhengyu Bai** is an associate professor at School of Chemistry and Chemical Engineering at Henan Normal University. She received her Ph.D. in 2010 from Henan Normal University. She received the Distinguished Young Investigator Awards at the 4th International Conference on Electrochemical Energy Science and Technology 2018 (EEST 2018). Her research is focused on new green energy nanomaterials, such as nanostructured electrocatalysts for fuel cell and metal-air batteries. Dr. Bai has published over 56 peer-reviewed journal articles. She is also listed as an inventor on 25 national patents, with 8 patents licensed in China.

Tao Zhang is a Ph.D. candidate in Institute of Advanced Materials, Nanjing Tech University and now he is an exchange student in Argonne National Laboratory. His research interests include energy materials (battery materials, catalytic materials), nanomaterials, and electrochemistry.

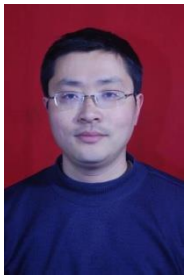

Dr. **Xiaobing Wang** is Associate Professor of the School of Chemistry and Chemical Engineering, Henan Normal University, Xinxiang, Henan, P. R. China. He received Ph.D. degree in Physical Chemistry in the group of L. Yang from Henan Normal University in 2016. Current research in his laboratory is focused on nanostructured and nanocomposite materials for use in energy storage, structural and multifunctional applications.

Dr. **Xiao-li Yang** is an associate Professor of Chemistry at Henan Normal University. She received her Ph.D. from Nanjing University (2010) with a major research on functional coordination compounds. Her current research interest is in the field of nanoscale coordination chemistry and materials, focusing on inorganic materials derived from coordination compounds and applied for clean environment and energy.

Xiaoming Ma is a Professor of Chemistry at Henan Normal University. She received her Ph.D. degree in Chemistry from Xiamen University, China in 2006. Her research interests include synthesis, properties and applications of functional nanomaterials with hierarchical structures.

Yuping Zhang received his Ph.D. in 2003 at the University of Science and Technology of China. He then worked as a postdoctoral fellow at Kyungpook National University, South Korea and a visiting scholar at Brigham Young University, USA. Currently, he is a professor at the Henan Institute of Science and Technology. His research interests focus on preparation and application of novel materials.

Dr. **Lin Yang** is a professor, Ph.D. supervisor and academic leader at Henan Normal University, China. He received his Ph.D. in Physical Chemistry from Lanzhou Institute of Chemical Physics of CAS. Dr. Yang is the vice president of Henan Normal University from 2008 and the associate director of the Key Laboratory of Green Chemical Media and Reactions, Ministry of Education. He was engaged in scientific research in Germany at TU Braunschweig during 1989-1991, and at University of Halle during 1994-1995. The technical expertise areas of Dr. Yang are new materials of electrochemical energy and inorganic/organic hybrid nanomaterials.

Dr. **Jun Lu** is a chemist at Argonne National Laboratory. His research interests focus on electrochemical energy storage and conversion technology, with the main focus on technology beyond Li-ion batteries. He received his bachelor degree in chemistry physics from the University of Science and Technology of China (USTC) in 2000. He completed his Ph.D. in material science from the Department of Metallurgical Engineering at the University of Utah in 2009. Following a DOE-EERE postdoctoral fellowship under Vehicles Technology Program, he joined the Division of Chemical Sciences and Engineering at Argonne National Laboratory as a chemist in 2015.